LANGMUIR Article
Cite This: Langmuir 2018, 34, 12609−12618
pubs.acs.org/Langmuir

Nonaqueous Microemulsion in the Bmim Tf_2N/Brij 30/*n*-Nonane System: Structural Investigation and Application as Gold Nanoparticle Microreactor

Marianna Mamusa, Marcia C. Arroyo, Emiliano Fratini, Rodorico Giorgi, and Piero Baglioni*

Department of Chemistry "Ugo Schiff" and CSGI, University of Florence, via della Lastruccia 3, Sesto Fiorentino, 50019 Florence, Italy

Supporting Information

ABSTRACT: Microemulsions based on ionic liquids (ILs) are being increasingly studied in many different areas of physical chemistry because of the attractive properties of ILs. In particular, waterless microemulsions where the IL represents the polar phase can be of interest for those applications that demand the nanosegregation of polar substances, but in which the absence of water is a strict requirement. In this work, we prepared a reverse, nonaqueous microemulsion based on the low-viscosity room-temperature IL, 1-butyl-3-methylimidazolium bis(trifluoromethylsulfonyl)-imide , the surfactant Brij 30, and *n*-nonane. The systems were characterized by dynamic light scattering and small-angle X-ray scattering; the IL/oil microemulsion was further employed as a templating system for the synthesis of gold nanoparticles from hydrogen tetrachloroaurate(III), $HAuCl_4$, by UV-photoreduction technique.

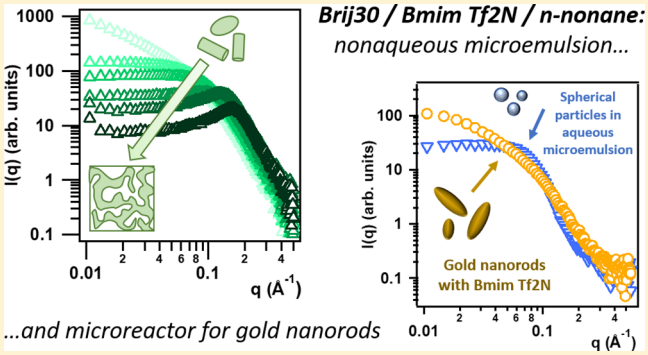

INTRODUCTION

An ionic liquid (IL) is a salt whose ions are sterically mismatched, resulting in these chemicals being in the liquid state below 100 °C or even at room temperature (room temperature ILs, RTILs).[1] These compounds possess many interesting features, such as extremely low vapor pressure, excellent solvation capabilities, high thermal stability, and good electrical conductivity.[2,3] Their physical−chemical properties, such as polarity, can be easily modulated by carefully choosing the ion pair and especially the anion, hence the common attribute of "designer solvents".[4] Interestingly, colloidal systems where ILs are combined with common surfactants display the same type of nanostructures and lyotropic phases known for aqueous and organic solvent-based mixtures.[5,6] The most extensively studied are protic ILs[7] such as ethylammonium nitrate (EAN), which is reminiscent of water in many aspects.[8] Self-assembly in EAN was demonstrated, among others, for systems containing polyoxyethylene non-ionic surfactants:[9,10] the associated phase diagrams reveal the presence of micellar phases as well as lamellar, cubic, and hexagonal mesophases. Self-assembly of both ionic and nonionic surfactants can take place in aprotic ILs as well: for example, C_iE_j surfactants,[11] Triton X-100,[12] Brij 35,[13] and sodium dodecyl sulfate (SDS)[14] form micelles in a whole range of imidazolium-based ILs, and the existence of surfactant vesicles in ILs has been reported.[15] Ternary systems have been also obtained, with the ILs playing the role of either the dispersing or the dispersed phase to form microemulsions.[16,17]

This is an especially interesting application of ILs: because of their distinctive physical−chemical properties, their use as microemulsion components may lead to the nanoconfined synthesis of new materials with interesting morphologies and properties that are not accessible using conventional organic solvents or water.[18,19] For example, there is a growing interest in the synthesis and stabilization of metal nanoparticles in IL-based microemulsions: this is especially true for ILs based on the imidazolium cation, which are known to play a crucial role as synthesis medium for various types of nanoparticles.[20−22] Hydrophobic ILs have been used as a polar oil to obtain microemulsions in aqueous systems.[23,24] Less frequently studied, but similarly interesting, are the systems where a hydrophobic IL is used to replace water as microemulsion component,[25−27] thereby providing a nonaqueous reaction medium for electrochemistry[28] or for the encapsulation of substances which have low affinity for both water and oils. One interesting imidazolium-based hydrophobic IL is 1-butyl-3-methylimidazolium bis(trifluoromethylsulfonyl)imide, Bmim Tf_2N (Scheme 1):[29] indeed, the Tf_2N anion is chosen more and more frequently for its robustness against hydrolysis compared to other fluorinated ILs,[30,31] and ILs carrying this anion have already been used to prepare nonaqueous direct,

Received: July 22, 2018
Revised: September 23, 2018
Published: September 28, 2018

DOI: 10.1021/acs.langmuir.8b02420
Langmuir 2018, 34, 12609−12618

Scheme 1. Chemical Structure of Bmim Tf_2N

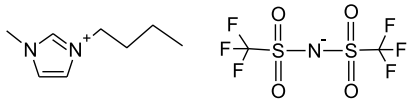

reverse, and bicontinuous microemulsions with different ionic and nonionic surfactants.[32−35]

Although the most investigated nonionic surfactant in these systems appears to be Triton X-100,[36−40] for this work we selected the polyoxyethylated lauryl ether [Brij 30, linear formula: $C_{12}H_{25}(OCH_2CH_2)_4OH$] and we explored the phase diagram for the Bmim Tf_2N/Brij 30/*n*-nonane system at 25 °C (see Figure 1). Samples in the microemulsion region were

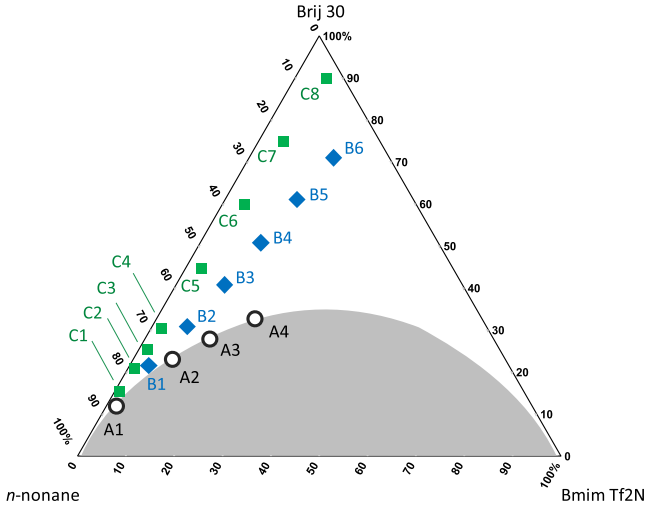

Figure 1. Ternary phase diagram of Bmim Tf_2N/Brij 30/*n*-nonane (in weight percentage) at 25 °C. The samples marked in the diagram were investigated by means of DLS and SAXS (see Table 1 for the exact compositions). The shadowed region corresponds to a multiphase area, whereas the one above represents the single-phase region.

prepared and characterized by means of dynamic light scattering (DLS) and small-angle X-ray scattering (SAXS). One of the most promising compositions was subsequently employed for the synthesis of gold nanoparticles via photo-induced reduction of Au(III) ions. Such nanoparticles were characterized and compared with colloidal gold synthesized in standard W/O microemulsions through UV−vis spectroscopy and SAXS techniques.

MATERIALS AND METHODS

Chemicals. *N*-Nonane (anhydrous, assay ≥99%), Brij 30, and $HAuCl_4·3H_2O$ (assay ≥99.9% trace metals basis) were purchased from Sigma-Aldrich. The IL Bmim Tf_2N (electrochemical grade, assay ≥99.5%) was purchased from Covalent Associates Inc. All reagents were used as received. The water used in this study was purified through a Milli-Q Plus system.

Sample Preparation. Samples for the determination of the ternary phase diagram for the Bmim Tf_2N/Brij 30/*n*-nonane system were prepared and stored in a water bath at 25 °C. Appropriate amounts of Bmim Tf_2N and Brij 30 were first added into glass test tubes, which were then supplemented with *n*-nonane and shaken using a vortex mixer. To better define and characterize the boundaries of the microemulsion region, further samples were prepared by weighing the appropriate amounts of Bmim Tf_2N and *n*-nonane into the glass test tubes; next, Brij 30 was added until the cloudy and milky mixture became completely clear, which is an indication of the existence of one single phase. No phase separation was observed over time, and all systems remained stable for at least 1 year.

Dynamic Light Scattering. Light scattering measurements were performed on a Brookhaven Instrument apparatus equipped with a BI9000AT correlator and a BI200SM goniometer. The signal was detected by an EMI 9863B/350 photomultiplier. The light source was the second harmonic of a diode-pumped Coherent Innova Nd:YAG laser (λ = 532 nm), linearly polarized in the vertical direction. Approximately 1 mL of sample solution was introduced into cylindrical scattering cells (Hellma) and analyzed at a scattering angle of 90°. All measurements were performed at 25 °C. The correlation function of scattering data was analyzed via the cumulant method to obtain the distribution of diffusion coefficients (D) of the solutes, and then the apparent hydrodynamic radius (R_{app}) was determined using the Stokes−Einstein law: $R_{app} = kT/6\pi\eta D$, where k is the Boltzmann constant, T the absolute temperature, and η the solvent's viscosity (in this case 0.6696 cP at 25 °C for *n*-nonane).

Small-Angle X-ray Scattering. SAXS experiments were performed on an S3-MICRO X-ray system by Hecus GMBH (Graz), equipped with an ultrabrilliant point microfocus source Genix-Fox 3D (Xenoxs, Grenoble). The impinging radiation was the 1.542 Å Cu Kα. The scattered X-rays were detected by a two-dimensional position sensitive detector, with a sample-to-detector distance of 281 mm. The primary beam was masked by a 2 mm W filter, positioned so that the region of scattering vector, q, was in the range $0.008 < q < 0.54$ Å^{-1}. Here, q has a modulus of $(4\pi/\lambda)\sin(\theta/2)$, with λ the X-ray wavelength (i.e., 1.542 Å) and θ the scattering angle. All measurements were collected at room temperature and with an X-ray source power of 50 W. Data modeling was carried out with the analysis suite developed at the NIST Center for Neutron Research.[41]

Briefly, in a SAXS experiment, the X-ray scattering intensity $I(q)$ is measured as a function of q. The measured scattered intensity per unit volume, for randomly oriented colloidal particles, is generally written as[42]

$$I(q) = K\varphi V_{part}(\Delta\rho)^2 P(q)S(q) \quad (1)$$

where K is an instrumental constant (not determined in the case of intensities in arbitrary units), φ is the volume fraction of the scattering particles, V_{part} is their scattering volume, $(\Delta\rho)^2$ is the contrast between the scattering length densities (SLDs) ρ of the solvent and the particles, $P(q)$ is the form factor, and $S(q)$ is the structure factor. $P(q)$ describes the scattering of individual particles and can yield information on their shape, especially when the structure factor can be neglected [$S(q) = 1$], as is the case for very dilute particle systems. When the particulate system is more concentrated, $S(q)$ describes the interference of scattering waves originated from the center of mass of different particles, and it can be used to gain information on the interaction potential existing among the scattering objects.[43]

SAXS curves in the dilute regime were modeled using a mathematical function representing the form factor of cylindrical objects[44]

$$P(q) = \frac{\varphi}{V_{cyl}}\int_0^{\pi/2} f^2(q, \alpha)\sin\alpha\, d\alpha \quad (2)$$

where the cylinder volume is

$$V_{cyl} = \pi R^2 L \quad (3)$$

and the scattering amplitude $f(q,\alpha)$ is a function the angle α between the cylinder axis and the q vector

$$f(q, \alpha) = 2(\rho_{cyl} - \rho_{solv})V_{cyl}j_0(qH\cos\alpha)\frac{J_1(qR\sin\alpha)}{(qR\sin\alpha)} \quad (4)$$

Here, $j_0(x) = \sin(x)/x$, and $J_1(x)$ is the first-order Bessel function.

SAXS patterns of concentrated samples were best treated according to the Teubner−Strey model[45]

DOI: 10.1021/acs.langmuir.8b02420
Langmuir 2018, 34, 12609−12618

$$I(q) = \frac{K}{a_2 + c_1 q^2 + c_2 q^4} + bkg \quad (5)$$

The values of the three fitting parameters a_2, c_1, and c_2 allow calculation of the periodicity, d, and the correlation length, ξ, of the microemulsion domains via eqs 6 and 7, respectively

$$\frac{d}{2\pi} = \left[\frac{1}{2}\left(\frac{a_2}{c_2}\right)^{1/2} - \frac{c_1}{4c_2}\right]^{-1/2} \quad (6)$$

$$\xi = \left[\frac{1}{2}\left(\frac{a_2}{c_2}\right)^{1/2} + \frac{c_1}{4c_2}\right]^{-1/2} \quad (7)$$

Synthesis of Gold Nanoparticles. IL/O and W/O microemulsions containing $HAuCl_4$ were prepared as follows: an aliquot of $HAuCl_4$ stock solution, either in IL or in water, was added into a micellar solution of Brij 30 in *n*-nonane. The volume fraction of the dispersed phase was the same for the IL-based and water-based microemulsions (φ = 1.3% vol). The final concentration of Au(III) was 7.4×10^{-4} mol/L in the IL/O microemulsion (Bmim Tf_2N 2.5% wt, Brij 30 15.5% wt, *n*-nonane 82.0% wt) and 4.6×10^{-4} mol/L in the W/O microemulsion (H_2O 1.7% wt, Brij 30 15.5% wt, and *n*-nonane 82.8% wt). The samples were placed in a water bath at the constant temperature of 25 °C. After equilibration for 7 days, an aliquot of 3.5 mL of each sample was taken in a 1 cm path length quartz cuvette for UV light irradiation with a 150 W Hg–Xe lamp for 30 min. Aliquots of both systems were taken and analyzed by DLS and SAXS upon 5 min UV exposure, and then every 5 min for absorbance measurements. UV–vis spectra were recorded with a Cary 100 spectrometer (Varian, Italy) in the 300–800 nm range.

RESULTS AND DISCUSSION

Phase Behavior of the Bmim Tf_2N/Brij 30/*n*-Nonane System at 25 °C. Figure 1 shows the ternary diagram representing the phase behavior of the Bmim Tf_2N/Brij 30/*n*-nonane system at 25 °C, determined by direct observation of the transition from turbidity to transparency. The binodal curve divides the diagram into a single-phase region above and a multiphase region below (shadowed area in the figure). A mixture whose overall composition lies within the single-phase region is most likely to correspond to a microemulsion. The shadowed area is a multiphase region, wherein a microemulsion phase coexists in equilibrium with excess *n*-nonane, excess Bmim Tf_2N, or both. As reported in previous works, it is observed that high surfactant concentrations are required to achieve a continuous stable single-phase microemulsion.[17,46,47]

Throughout a single-phase region in a triangular phase diagram, the microstructure can change dramatically as a function of composition,[48] from small oil droplets in water (or polar solvent) at high water content to reverse droplets on the oil-rich side, possibly passing through bicontinuous structures in the middle of the phase diagram.[49] As we are interested in the technological applications of the reverse IL/O microemulsion, a series of samples within the low IL-content area were chosen for microstructural characterization, in particular along the binodal curve ("A" series, evidenced in Figure 1 with circular markers). The one-phase region was further investigated by following two dilution lines: the "B" and "C" series (blue diamonds and green square symbols, respectively, in Figure 1) correspond to the dilution lines with surfactant-to-IL weight ratios of 80/20 and 93/7, respectively. The exact concentrations relative to all these samples are given in Table 1, along with the corresponding abbreviations that will be used throughout the text.

Table 1. Abbreviations and Compositions (% wt) of Samples Marked in Figure 1; "BTf2N" Stands for Bmim Tf_2N[a]

sample	Brij 30 (% wt)	Bmim Tf_2N (% wt)	*n*-nonane (% wt)	W_{IL}
A1 = Brij 30/BTf2N 10.8/2.4	10.8	2.4	86.8	0.13
A2 = Brij 30/BTf2N 23.5/7.5	23.5	7.5	69.0	0.18
A3 = Brij 30/BTf2N 29.0/12.5	29.0	12.5	58.5	0.24
A4 = Brij 30/BTf2N 33.2/19.4	33.2	19.4	47.4	0.33
B1 = Brij 30/BTf2N 20.0/5.0	20.0	5.0	75.0	0.14
B2 = Brij 30/BTf2N 30.0/7.5	30.0	7.5	62.5	0.14
B3 = Brij 30/BTf2N 40.0/10.0	40.0	10.0	50.0	0.14
B4 = Brij 30/BTf2N 50.0/12.5	50.0	12.5	37.5	0.14
B5 = Brij 30/BTf2N 60.0/15.0	60.0	15.0	25.0	0.14
B6 = Brij 30/BTf2N 70.0/17.5	70.0	17.5	12.5	0.14
C1 = Brij 30/BTf2N 15.0/1.0	15.0	1.0	84.0	0.04
C2 = Brij 30/BTf2N 20.0/1.5	20.0	1.5	78.5	0.04
C3 = Brij 30/BTf2N 25.0/2.0	25.0	2.0	73.0	0.04
C4 = Brij 30/BTf2N 30.0/2.3	30.0	2.3	67.7	0.04
C5 = Brij 30/BTf2N 45.0/3.5	45.0	3.5	51.5	0.04
C6 = Brij 30/BTf2N 60.0/4.5	60.0	4.5	35.5	0.04
C7 = Brij 30/BTf2N 75.0/5.5	75.0	5.5	19.5	0.04
C8 = Brij 30/BTf2N 90.0/7.0	90.0	7.0	3.0	0.04

[a] W_{IL} = [BTf2N]/[Brij 30].

The microstructure of the single-phase region was investigated by means of scattering techniques. For the samples that were fluid and isotropic, we used DLS to analyze the Brownian motion of the droplets[50] in *n*-nonane and extrapolate their diffusion coefficients, D. Apparent hydrodynamic radii (R_{app}) and size distribution were obtained through the Stokes–Einstein law, $R_{app} = kT/6\pi\eta D$. The measured DLS curves are shown in Supporting Information (Figure S1); the experimental data, consistent with a single relaxation time of the field autocorrelation, were analyzed using the cumulant method,[51] and the results are summarized in Table 2.

For the "A" series, situated on the binodal curve of the phase diagram, the average hydrodynamic radii (R_{app}) were comprised between ~10 and 30 nm. For the samples of the other two series "B" and "C", DLS measurements suggested the formation of very small droplets. Indeed, radii were in the range of 1.5–4 nm, except for sample B1 (Brij 30/BTf_2N 20.0/5.0), which showed about the same droplet size as sample A2 (Brij 30/BTf_2N 23.5/7.5). A general trend toward larger droplets size, that is, a swelling behavior, was observed for samples lying along the binodal curve as a function of the [BTf2N]/[Brij 30] ratio, W_{IL}. However, such behavior did not follow a linear trend, which could suggest nonspherical droplet

DOI: 10.1021/acs.langmuir.8b02420
Langmuir 2018, 34, 12609–12618

Table 2. Apparent Hydrodynamic Radii (R_{app}, nm) and Associated Polydispersity Indexes for Bmim Tf_2N/Brij 30/*n*-Nonane Systems ("BTf2N" Stands for Bmim Tf_2N), Deduced from DLS Measurements through Fitting of the Autocorrelation Functions with the Cumulant Method[a]

sample	W_{IL}	R_{app} (nm)	PDI
A1 = Brij 30/BTf2N 10.8/2.4	0.13	9.6	0.09
A2 = Brij 30/BTf2N 23.5/7.5	0.18	20.4	0.08
A3 = Brij 30/BTf2N 29.0/12.5	0.24	17.8	0.10
A4 = Brij 30/BTf2N 33.2/19.4	0.33	29.7	0.20
B1 = Brij 30/BTf2N 20.0/5.0	0.14	23.9	0.08
B2 = Brij 30/BTf2N 30.0/7.5	0.14	3.6	0.22
C1 = Brij 30/BTf2N 15.0/1.0	0.04	1.9	0.35
C2 = Brij 30/BTf2N 20.0/1.5	0.04	1.7	0.29
C3 = Brij 30/BTf2N 25.0/2.0	0.04	1.7	0.26
C4 = Brij 30/BTf2N 30.0/2.3	0.04	2.2	0.11
C5 = Brij 30/BTf2N 45.0/3.5	0.04	1.6	0.34

[a]DLS analysis was performed only on those samples that presented a scattering intensity at least 10 times higher than the pure solvent. W_{IL} = [BTf2N]/[Brij 30].

shape and/or the existence of interparticle interactions.[52] For the samples located on both dilution lines, which have very low W_{IL} values, droplets' size decreased drastically, whereas polydispersity increased with the concentrations of both constituents. This seems to hint at the presence of a higher number of microemulsion droplets; yet some care has to be taken when interpreting fitting results for broadly polydisperse samples, keeping in mind that the cumulant method assumes particle size distribution to be unimodal and monodisperse, that is, with polydispersity index (PDI) below a value of 0.1. Generally speaking, for samples with a slightly increased PDI than 0.1, results should be confirmed using other techniques, whereas for broader distributions, where the polydispersity is over 0.2, it is unwise to rely on the average mean.[53] In addition, DLS yields a diffusion coefficient, from which the equivalent rigid sphere radius can be inferred and, as such, it provides no information about particle shape. The hydrodynamic radius for nonspherical objects with the same volume may strongly vary depending upon shape. Thus, for a better evaluation of the microemulsion nanostructure, SAXS was used to obtain further information on the nanostructure of microemulsion droplets.

Figure 2 summarizes the SAXS patterns obtained for all the samples listed in Table 1. For each series, a tendency toward lower $I(0)$ scattering intensity is evident for increasing total surfactant and IL concentrations in nonane at constant W_{IL}. The curves in (panel a) (samples along the binodal line in the phase diagram) present a q^{-1} slope in the low q region, suggesting the existence of elongated scattering objects. A similar appearance is presented by the more dilute samples of series B and C. Furthermore, along these two dilution lines a prominent structure peak appears mid-series and becomes more pronounced as the Brij 30/BTf2N concentration in nonane approaches the binary axis. In order to shed more light on the nanostructures found in this phase diagram, we will discuss the "dilute" and concentrated regimes separately.

We were able to evidence that the surfactant shell around the IL core is not addressable because of the nature of the probe−sample interaction as follows. Table 3 shows the SLDs

Table 3. SLDs (ρ) of the Different Constituents of the Bmim Tf_2N/Brij 30/*n*-Nonane System, Obtained from Molecular Considerations of Each Component

	ρ (Å^{-2})
nonane (ρ_S)	7.00×10^{-6}
Brij 30 tail (ρ_{TG})	6.41×10^{-6}
Brij 30 headgroup (ρ_{HG})	1.05×10^{-5}
Bmim Tf_2N (ρ_{IL})	1.26×10^{-5}

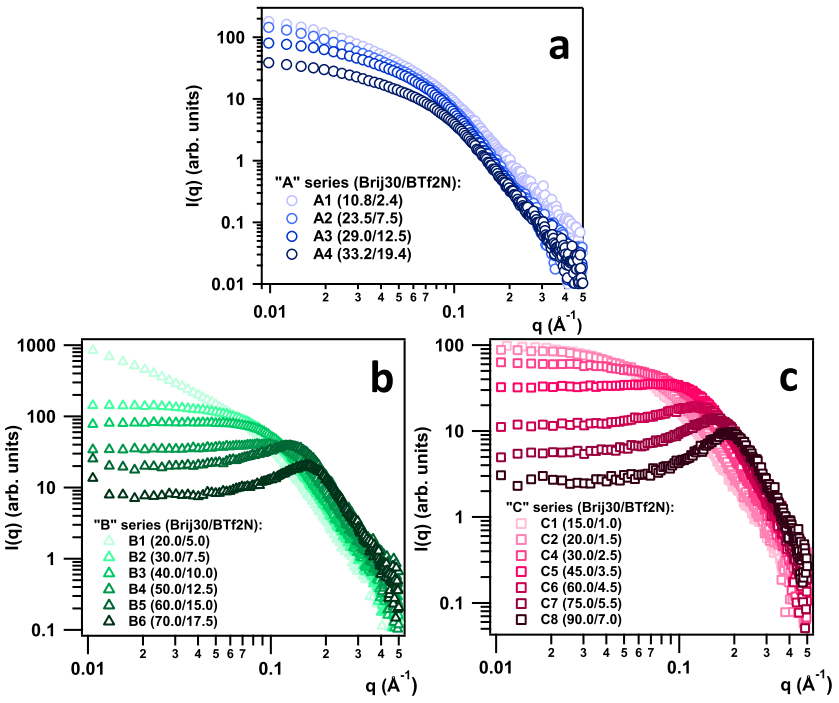

Figure 2. SAXS patterns obtained for the three samples series listed in Table 1. (Panel a) "A" series; (panel b) "B" series; (panel c) "C" series. Please refer to legends in each panel for compositions and to Figure 1 to locate series A, B, and C.

DOI: 10.1021/acs.langmuir.8b02420
Langmuir 2018, 34, 12609−12618

(ρ) of the different constituents of the Bmim Tf_2N/Brij 30/*n*-nonane system, obtained from the molecular structure and volumes of each species. In particular, the surfactant headgroups and tails are considered separately because of the different electron-rich and electron-poor moieties. It can be noticed that the SLDs of the IL and of the surfactant headgroup are very close, so that we will not be able to resolve the surfactant shell from the IL core. Hence, as is customary for heterogeneous particles of this type,[54] we can assume the total ρ of the particle core to be the average over those of the IL and the surfactant headgroup. Similarly, the contrast between solvent and Brij 30 hydrocarbon tails is too small to resolve a shell structure, and both constituents are therefore expected to contribute to the total ρ of the solvent. A pictorial representation of this situation is given in Scheme 2.

Scheme 2. Schematic Representation of the SLD Profiles of the Microemulsion Droplets, with $\rho_{IL} \approx \rho_{HG}$ (Dark Areas) and $\rho_{Solvent} \approx \rho_{TG}$ (Light Areas), as per Eqs 8 and 9

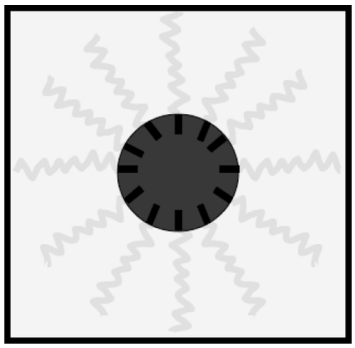

On the basis of such reasoning, and using the ρ values given in Table 3, for each sample we calculated the volume fraction-weighted average SLD of the droplet, $\overline{\rho}_{particle}$, and of the dispersing phase, $\overline{\rho}_{solvent}$, according to eqs 8 and 9[54]

$$\overline{\rho}_{particle} = \phi_{IL}\rho_{IL} + (1 - \phi_{IL})\rho_{HG} \quad (8)$$

$$\overline{\rho}_{solvent} = \phi_{S}\rho_{S} + (1 - \phi_{S})\rho_{TG} \quad (9)$$

where ϕ_{IL} and ϕ_S represent the volume fractions of the IL and the solvent, respectively. Subscripts IL, S, HG, and TG refer respectively to the IL, the solvent, the surfactant headgroup, and the surfactant tail group.

SAXS patterns shown in Figure 3 pertain to the "dilute" regime region of the reverse Bmim Tf_2N/Brij 30/*n*-nonane microemulsion. Best fits were obtained using a form factor representing the scattering from cylindrical objects (eq 2); the introduction of polydispersity (Schulz distribution) on the cylinder radius was necessary to obtain reliable fits at high q values.

Table 4 summarizes the best fit values for cylinder radius, radial polydispersity, and cylinder length, obtained by modeling the experimental data with eq 2: fitting results showed an apparent decreasing trend in cylinder length as Brij 30 weight fraction increased, whereas radial polydispersity, which corresponds to the root-mean-square deviation (σ) from the mean cylinder−core radius, showed values ranging between 0.23 and 0.47. Such decreasing trend is counter-intuitive; in order to explain it, we must notice that the present modeling procedure did not take into account any structure factor. Indeed, considering that the concentrated samples (see Figure 2) present a marked structure peak, it is likely that the SAXS patterns of these dilute samples are also affected by interparticle interactions even if to a low degree, which would

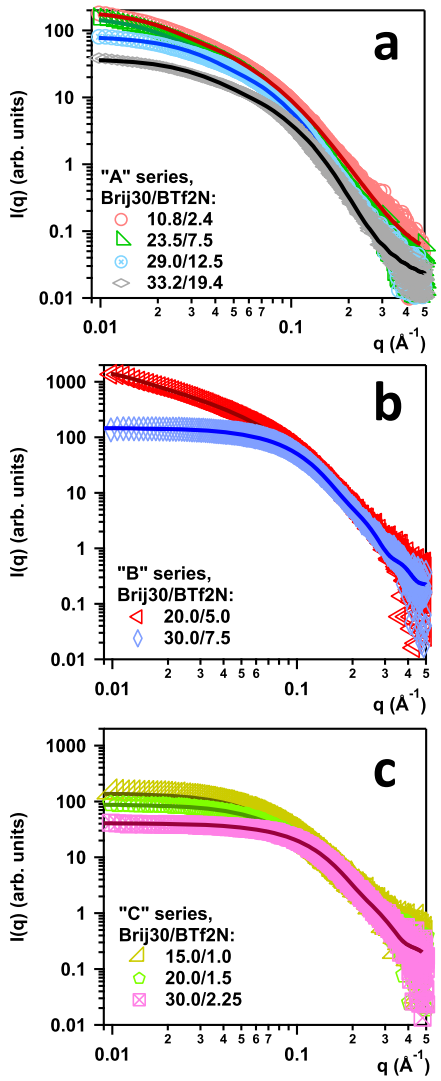

Figure 3. SAXS curves, obtained at 25 °C, of some Bmim Tf_2N/Brij 30/*n*-nonane mixtures. (Panel a) "A" series; (panel b) "B" series; (panel c) "C" series. Please refer to legends in each panel for compositions and to Figure 1 to locate series A, B, and C.

Table 4. Parameter Values Derived from SAXS Data Modeling in Dependence of the Composition of the Microemulsion as Reported in Figure 1[a]

sample	W_{IL}	R (nm)	σ	L (nm)
A1 = Brij 30/BTf2N 10.8/2.4	0.13	0.7	0.8	22.5
A2 = Brij 30/BTf2N 23.5/7.5	0.18	1.2	0.4	24.8
A3 = Brij 30/BTf2N 29.0/12.5	0.24	1.4	0.3	14.8
A4 = Brij 30/BTf2N 33.2/19.4	0.33	1.2	0.3	13.8
B1 = Brij 30/BTf2N 20.0/5.0	0.14	0.9	0.4	54.6
B2 = Brij 30/BTf2N 30.0/7.5	0.14	1.0	0.4	4.3
C1 = Brij 30/BTf2N 15.0/1.0	0.04	0.8	0.4	8.1
C2 = Brij 30/BTf2N 20.0/1.5	0.04	0.8	0.4	6.3
C3 = Brij 30/BTf2N 25.0/2.0	0.04	0.8	0.4	3.5

[a] W_{IL} = [BTf2N]/[Brij 30]; R = cylinder radius (nm); σ = radial polydispersity according to a Schulz distribution of radii; L = cylinder length (nm).

DOI: 10.1021/acs.langmuir.8b02420
Langmuir 2018, 34, 12609−12618

account for the fact that the scattering objects appear to shrink with increasing surfactant concentration. However, introducing $S(q)$ in the modeling would complicate the procedure because of the elevated polydispersity in many of the samples: indeed, in such a situation, the decoupling approximation[43] is not valid and we would need to consider the polydispersity for $P(q)$ and $S(q)$ separately. Moreover, most available structure factor models are based on spherical symmetry and not applicable to cylindrical objects.

In order to evaluate the agreement between results from SAXS and DLS, the radius of gyration R_g can be compared to the apparent hydrodynamic radius R_{app}. Table 5 reports R_g values determined from SAXS data using the Guinier approximation. As previously described, in a noninteracting or dilute system the structure factor is equal to 1 and particle shape can be determined from the form factor $P(q)$. In the low q-region, only at the very beginning of the scattering curve ($qR_g < 1.3$),[42] $P(q)$ decreases exponentially and the Guinier approximation can be applied[43]

Table 5. W_{IL} = [BTf2N]/[Brij 30], R_{app} (Apparent Hydrodynamic Radius), and R_g (Gyration Radius) Values in Dependence of the Composition of the Microemulsion, for Some of the Samples Reported in Figure 1

sample	W_{IL}	R_{app} (nm)	R_g (nm)
A1 = Brij 30/BTf2N 10.8/2.4	0.13	9.6	7.1
A2 = Brij 30/BTf2N 23.5/7.5	0.18	20.4	6.9
A3 = Brij 30/BTf2N 29.0/12.5	0.24	17.8	4.9
B1 = Brij 30/BTf2N 20.0/5.0	0.14	23.9	10.0
B2 = Brij 30/BTf2N 30.0/7.5	0.14	3.6	1.7
C1 = Brij 30/BTf2N 15.0/1.0	0.04	1.9	2.9
C2 = Brij 30/BTf2N 20.0/1.5	0.04	1.7	2.4
C4 = Brij 30/BTf2N 30.0/2.3	0.04	2.2	1.4

$$P(q) = \exp\left(-\frac{q^2 R_g^{\,2}}{5}\right) \tag{10}$$

For rod particles, the radius of gyration of the cross section, R_g, and thus the radius, R, of the particle, can be derived.[55] Within the limit $ql \gg 1 \gg qR$, where l is the cylinder length, $P(q)$ decreases exponentially as[42]

$$P(q) = \frac{\pi}{2ql} \exp\left(-\frac{q^2 R^2}{4}\right) \tag{11}$$

Thus, the radius R of the cylindrical particle can be obtained from the slope of the so-called cross-sectional Guinier plot: $\ln[P(q)q]$ versus q^2. However, it is worth noting that cross-sectional Guinier plots did not show a linear relationship within the Guinier region: this is considered as being because of the large distribution of domain sizes and implies that we must take into account the limitation of the Guinier method for the analysis of polydisperse systems.

Observing the results reported in Table 5, one can notice that R_{app} values are in general larger than R_g. This is explained considering that the radius obtained from the diffusional properties of the particle is indicative of the size of the dynamic solvated particle, whereas SAXS is a static method sensitive to the topological radius.[56] By definition, R_g is the root-mean-square distance of all scattering elements from the center of gravity; therefore, the hydrodynamic radius is often larger than the topological one. Moreover, as previously described, because of their similar SLDs we expected the surfactant tail group to contribute to the total SLD of the solvent; hence, the SAXS particle sizes represent only the polar cores of the reverse microemulsion.

SAXS curves pertaining to the systems with high surfactant content are shown in Figure 4. We can observe that increasing surfactant and IL concentration leads to a decrease of the scattering intensity at low q. At the same time, a faint peak develops, which becomes more pronounced and moves slightly toward larger q values.

The Teubner–Strey model[45] (eq 5), developed for bicontinuous structures, well describes the broad scattering peak and the q^{-4} decay at large q. Using this function to fit the experimental SAXS data allowed us to calculate the nanoscale features of the microemulsion structure, namely, the average interdomain distance between two water or oil domains (the periodicity), d, and the correlation length, ξ. The ratio d/ξ measures the polydispersity of the domain sizes: the smaller this ratio, the more ordered the system. Thus, d/ξ is expected to decrease with surfactant concentration.[45,57] In addition, calculation of f_a (eq 12) allows the location of individual samples on a scale of relative amphiphilicity.[58]

$$f_a = \frac{c_1}{\sqrt{4a_2c_2}} \tag{12}$$

The value of f_a[57,59,60] amounts to 1 for the disorder line, where the solution loses its quasiperiodical order; the liquid crystalline lamellar phase corresponds to $f_a = -1$. These values define the region where microemulsions may be found. The

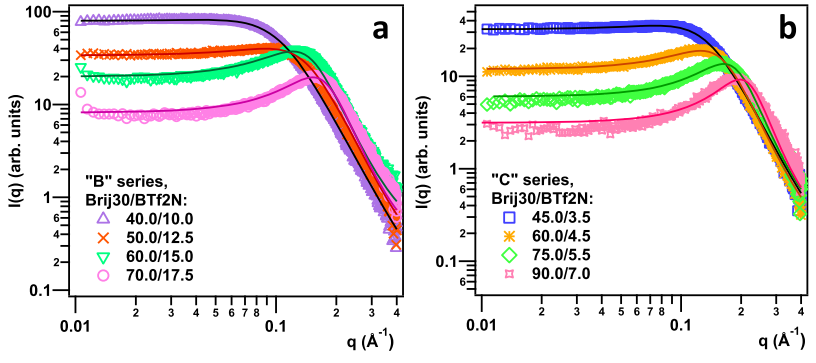

Figure 4. SAXS curves of Bmim Tf2N/Brij 30/*n*-nonane mixtures at 25 °C with increasing IL and surfactant content. (Panel a) "B" series; (panel b) "C" series (see also Figure 1).

DOI: 10.1021/acs.langmuir.8b02420
Langmuir 2018, 34, 12609−12618

factor ranges between −0.9 and −0.7 for well-structured bicontinuous microemulsions. The Lifshitz and the disorder lines may be taken as demarcation lines for the transition from weakly structured mixtures to genuine microemulsions.

Table 6 summarizes the fit values of the c_1 coefficients, the periodicity d, the correlation length ξ, the disorder parameter d/ξ, and the amphiphilic factor f_a. The c_1 values are negative, as expected when a correlation peak develops in the scattering intensity curves.[61] Accordingly, the f_a of our samples remains negative as a function of surfactant and IL concentration, indicating that systems correspond to an ordered microemulsion. Moreover, f_a values decrease by increasing surfactant Brij 30 concentration, showing the progression to more strongly structured mixtures.

Table 6. c_1 Coefficient Values from the Teubner−Strey Model Fitting (Eq 5); ξ, d, d/ξ, and f_a Derived from the Fit Results

sample	c_1	ξ (nm)	d (nm)	d/ξ	f_a
B3 = Brij 30/BTf2N 40.0/10.0	−0.35	14.6	78.5	5.4	−0.15
B4 = Brij 30/BTf2N 50.0/12.5	−1.23	13.2	55.0	4.2	−0.39
B5 = Brij 30/BTf2N 60.0/15.0	−2.79	15.9	43.3	2.7	−0.68
B6 = Brij 30/BTf2N 70.0/17.5	−5.63	15.8	36.0	2.3	−0.77
C5 = Brij 30/BTf2N 45.0/3.5	−0.97	12.3	57.1	4.7	−0.29
C6 = Brij 30/BTf2N 60.0/4.5	−3.96	14.0	43.6	3.1	−0.61
C7 = Brij 30/BTf2N 75.0/5.5	−7.24	15.0	35.6	2.4	−0.75
C8 = Brij 30/BTf2N 90.0/7.0	−11.8	15.4	30.3	2.0	−0.82

Microemulsion Templates for the Synthesis of Au Nanoparticles. The reverse IL/oil microemulsions were investigated as templating systems for the synthesis of gold nanoparticles by UV-photoreduction of tetrachloroaurate(III), $HAuCl_4$.[62] The tested IL-containing microemulsion had the following composition: Bmim Tf_2N/Brij 30/*n*-nonane 2.5/15.5/82% wt, with $HAuCl_4$ concentration of 7.4×10^{-4} mol/L. The formation of gold nanoparticles was monitored using UV−vis absorption spectroscopy, and the suspensions were characterized by DLS and SAXS. For comparison, we performed the same reaction in an aqueous microemulsion of composition H_2O/Brij 30/*n*-nonane 1.8/15.5/82.7% wt, containing 4.6×10^{-4} mol/L $HAuCl_4$. The chemical reactivity within the reverse microemulsions was compared to that in the respective bulk phases, where $HAuCl_4$ was dissolved in Bmim Tf_2N and water at the concentrations of 1.1×10^{-3} and 1.4×10^{-3} mol/L, respectively.

After a brief (5 min) exposure to UV light, the color of the Bmim Tf_2N-based microemulsion turned slightly blue-purple, whereas the aqueous microemulsion produced a pink sol. Figure 5 shows the UV−vis absorbance spectra recorded for the abovementioned systems after an exposure to UV light of 10 min. Evidently, the optical spectra present the typical plasmon resonance signature of gold sols, around 540 nm, which instead is absent in the samples where chloroauric acid is simply dissolved in either IL or water.

The nanoscale morphology of the particles obtained in both types of microemulsion was evaluated through SAXS analysis of the systems, presented in Figure 6. The experimental data pertaining to the IL/O system were modeled using the same cylinder form factor as previously in this work, where the SLD of the cylinder (2.6×10^{-5} Å^{-2}) was calculated considering the gold-to-IL ratio. Curve fitting yielded a radius of 1.1 nm with polydispersity σ = 0.48, and a cylinder length of 28.0 nm, consistent with droplet sizes obtained previously (Table 4). The aqueous microemulsion data were fitted using a sphere form factor with Schulz distribution of the radii and considering a hard-spheres repulsive potential between particles. The particle ρ was weighed on the gold/water volume fraction. As a result, the average particle radius was found to be 2.7 nm, with polydispersity σ = 0.2. Hence, both microemulsions can be assumed to be very efficient templates for controlling particle size and shape: gold nanoparticles obtained from the IL/O microemulsion are cylindrical, whereas those obtained from the W/O microemulsion are spherical in shape.

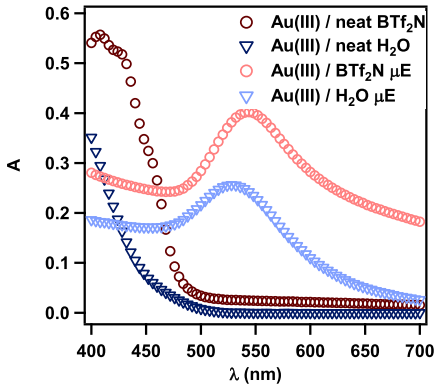

Figure 5. UV−vis absorption spectra, after 10 min of UV irradiation, of gold in Bmim Tf_2N (dark red circles); water (dark blue triangles); IL/O microemulsion (light red circles); and W/O microemulsion (light blue triangles).

CONCLUSIONS

In this work, we obtained nonaqueous, reverse microemulsions in which the polar core of the droplets is constituted by the RTIL Bmim Tf_2N, stabilized by the surfactant Brij 30 in *n*-nonane. We investigated the phase behavior and the microstructure of the ternary system using DLS and SAXS, which allowed for the identification of two structural regimes in the IL/O microemulsion region. For low surfactant concentrations, discrete IL droplets of cylindrical shape are formed with an average radius of approximately 1−1.5 nm. The IL is likely to intercalate among the polar headgroups of the surfactant, modifying its effective packing parameter[63] and inducing the formation of cylindrical structures instead of the spherical ones found for the water-in-nonane microemulsion. As the Brij 30 content increases, a percolation behavior is observed toward the formation of a bicontinuous microemulsion. These results are consistent with other reports in which nonaqueous microemulsions, discrete and bicontinuous, are described in the presence of a fluorinated IL stabilized by a nonionic surfactant in oil.[36−38]

The reverse Bmim Tf_2N/Brij 30/*n*-nonane microemulsion was used for the first time as a nanoreactor to perform the synthesis of gold nanoparticles. The formation of Au nanoparticles was monitored using UV−vis absorption spectroscopy. Nanoparticles were then characterized using SAXS,

DOI: 10.1021/acs.langmuir.8b02420
Langmuir 2018, 34, 12609−12618

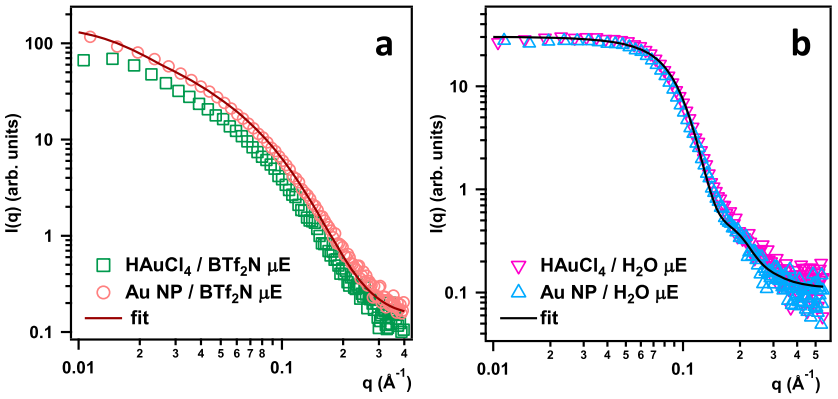

Figure 6. SAXS curves at 25 °C. (a) IL-based microemulsions containing Au salt (green squares) and Au nanoparticles (red circles) obtained after a 5′ exposure to UV light. (b) Water-based microemulsions containing Au salt (pink downwards triangles) and Au nanoparticles (blue upwards triangles) obtained after a 5′ exposure to UV light. In both panels, solid lines are fits to the Au NP-containing microemulsion curves.

resulting cylindrical-shaped as expected from the droplet shape observed in the low-surfactant regime microemulsion template. For comparison, gold nanoparticles were prepared in a classical W/O microemulsion, and they were spherical in shape and more polydisperse; however, they presented a better colloidal stability. Further investigation of the effect of different parameters on the synthesis of gold nanoparticles in the IL-in-oil microemulsion will take place in order to achieve a better understanding of the optimal synthesis conditions using the present method.

■ ASSOCIATED CONTENT

Supporting Information

The Supporting Information is available free of charge on the ACS Publications website at DOI: 10.1021/acs.langmuir.8b02420.

DLS data (PDF)

■ AUTHOR INFORMATION

Corresponding Author

*E-mail: piero.baglioni@unifi.it. Phone: +39 055 457 3033.

ORCID

Marianna Mamusa: 0000-0002-4344-9786

Emiliano Fratini: 0000-0001-7104-6530

Piero Baglioni: 0000-0003-1312-8700

Notes

The authors declare no competing financial interest.

■ ACKNOWLEDGMENTS

The authors are grateful to Prof. Debora Berti (University of Florence, Italy) for fruitful discussions. The authors kindly acknowledge partial financial support from Consorzio Interuniversitario per lo Sviluppo dei Sistemi a Grande Interfase (CSGI).

■ REFERENCES

(1) Krossing, I.; Slattery, J. M.; Daguenet, C.; Dyson, P. J.; Oleinikova, A.; Weingärtner, H. Why Are Ionic Liquids Liquid? A Simple Explanation Based on Lattice and Solvation Energies. *J. Am. Chem. Soc.* **2006**, *128*, 13427−13434.

(2) Aparicio, S.; Atilhan, M.; Karadas, F. Thermophysical Properties of Pure Ionic Liquids: Review of Present Situation. *Ind. Eng. Chem. Res.* **2010**, *49*, 9580−9595.

(3) Ghandi, K. A Review of Ionic Liquids, Their Limits and Applications. *Green Sustainable Chem.* **2014**, *04*, 44−53.

(4) Ab Rani, M. A.; Brant, A.; Crowhurst, L.; Dolan, A.; Lui, M.; Hassan, N. H.; Hallett, J. P.; Hunt, P. A.; Niedermeyer, H.; Perez-Arlandis, J. M.; et al. Understanding the Polarity of Ionic Liquids. *Phys. Chem. Chem. Phys.* **2011**, *13*, 16831.

(5) *Ionic Liquid-Based Surfactant Science: Formulation, Characterization and Applications*; Paul, B. K., Moulik, S. P., Eds.; Wiley Series on Surface and Interfacial Chemistry; John Wiley & Sons: Hoboken, New Jersey, 2015.

(6) Hao, J.; Zemb, T. Self-Assembled Structures and Chemical Reactions in Room-Temperature Ionic Liquids. *Curr. Opin. Colloid Interface Sci.* **2007**, *12*, 129−137.

(7) Greaves, T. L.; Drummond, C. J. Protic Ionic Liquids: Evolving Structure-Property Relationships and Expanding Applications. *Chem. Rev.* **2015**, *115*, 11379−11448.

(8) Evans, D. F.; Yamauchi, A.; Roman, R.; Casassa, E. Z. Micelle Formation in Ethylammonium Nitrate, a Low-Melting Fused Salt. *J. Colloid Interface Sci.* **1982**, *88*, 89−96.

(9) Araos, M. U.; Warr, G. G. Structure of Nonionic Surfactant Micelles in the Ionic Liquid Ethylammonium Nitrate. *Langmuir* **2008**, *24*, 9354−9360.

(10) Araos, M. U.; Warr, G. G. Self-Assembly of Nonionic Surfactants into Lyotropic Liquid Crystals in Ethylammonium Nitrate, a Room-Temperature Ionic Liquid. *J. Phys. Chem. B* **2005**, *109*, 14275−14277.

(11) Patrascu, C.; Gauffre, F.; Nallet, F.; Bordes, R.; Oberdisse, J.; de Lauth-Viguerie, N.; Mingotaud, C. Micelles in Ionic Liquids: Aggregation Behavior of Alkyl Poly(Ethyleneglycol)-Ethers in 1-Butyl-3-Methyl-Imidazolium Type Ionic Liquids. *ChemPhysChem* **2006**, *7*, 99−101.

(12) Selwent, A.; Łuczak, J. Micellar Aggregation of Triton X-100 Surfactant in Imidazolium Ionic Liquids. *J. Mol. Liq.* **2016**, *221*, 557−566.

(13) Tran, C. D.; Yu, S. Near-Infrared Spectroscopic Method for the Sensitive and Direct Determination of Aggregations of Surfactants in Various Media. *J. Colloid Interface Sci.* **2005**, *283*, 613−618.

(14) Anderson, J. L.; Pino, V.; Hagberg, E. C.; Sheares, V. V.; Armstrong, D. W. Surfactant Solvation Effects and Micelle Formation in Ionic Liquids. *Chem. Commun.* **2003**, 2444.

(15) Rao, K. S.; So, S.; Kumar, A. Vesicles and Reverse Vesicles of an Ionic Liquid in Ionic Liquids. *Chem. Commun.* **2013**, *49*, 8111.

(16) Kunz, W.; Zemb, T.; Harrar, A. Using Ionic Liquids to Formulate Microemulsions: Current State of Affairs. *Curr. Opin. Colloid Interface Sci.* **2012**, *17*, 205−211.

(17) Gao, H.; Li, J.; Han, B.; Chen, W.; Zhang, J.; Zhang, R.; Yan, D. Microemulsions with Ionic Liquid Polar Domains. *Phys. Chem. Chem. Phys.* **2004**, *6*, 2914.

DOI: 10.1021/acs.langmuir.8b02420
Langmuir 2018, 34, 12609−12618

(18) Taubert, A.; Li, Z. Inorganic Materials from Ionic Liquids. *Dalton Trans.* **2007**, 723−727.
(19) Zhao, M.; Zheng, L.; Bai, X.; Li, N.; Yu, L. Fabrication of Silica Nanoparticles and Hollow Spheres Using Ionic Liquid Microemulsion Droplets as Templates. *Colloids Surf., A* **2009**, *346*, 229−236.
(20) Ma, Z.; Yu, J.; Dai, S. Preparation of Inorganic Materials Using Ionic Liquids. *Adv. Mater.* **2010**, *22*, 261−285.
(21) Chen, H. M.; Liu, R.-S. Architecture of Metallic Nanostructures: Synthesis Strategy and Specific Applications. *J. Phys. Chem. C* **2011**, *115*, 3513−3527.
(22) Neouze, M.-A. About the Interactions between Nanoparticles and Imidazolium Moieties: Emergence of Original Hybrid Materials. *J. Mater. Chem.* **2010**, *20*, 9593.
(23) Porada, J. H.; Mansueto, M.; Laschat, S.; Stubenrauch, C. Microemulsions with Novel Hydrophobic Ionic Liquids. *Soft Matter* **2011**, *7*, 6805.
(24) Sun, Y.; Yan, K.; Huang, X. Formation, Characterization and Enzyme Activity in Water-in-Hydrophobic Ionic Liquid Microemulsion Stabilized by Mixed Cationic/Nonionic Surfactants. *Colloids Surf., B* **2014**, *122*, 66−71.
(25) Falcone, R. D.; Correa, N. M.; Silber, J. J. On the Formation of New Reverse Micelles: A Comparative Study of Benzene/Surfactants/Ionic Liquids Systems Using UV−Visible Absorption Spectroscopy and Dynamic Light Scattering. *Langmuir* **2009**, *25*, 10426−10429.
(26) Sarkar, S.; Pramanik, R.; Ghatak, C.; Rao, V. G.; Sarkar, N. Characterization of 1-ethyl-3-methylimidazolium bis-(trifluoromethylsulfonyl)imide ([Emim][Tf2N])/TX-100/cyclohexane ternary microemulsion: Investigation of photoinduced electron transfer in this RTIL containing microemulsion. *J. Chem. Phys.* **2011**, *134*, 074507.
(27) Zech, O.; Kunz, W. Conditions for and Characteristics of Nonaqueous Micellar Solutions and Microemulsions with Ionic Liquids. *Soft Matter* **2011**, *7*, 5507.
(28) Fu, C.; Zhou, H.; Wu, H.; Chen, J.; Kuang, Y. Research on Electrochemical Properties of Nonaqueous Ionic Liquid Microemulsions. *Colloid Polym. Sci.* **2008**, *286*, 1499−1504.
(29) Xue, H.; Verma, R.; Shreeve, J. M. Review of Ionic Liquids with Fluorine-Containing Anions. *J. Fluorine Chem.* **2006**, *127*, 159−176.
(30) Swatloski, R. P.; Holbrey, J. D.; Rogers, R. D. Ionic Liquids Are Not Always Green: Hydrolysis of 1-Butyl-3-Methylimidazolium Hexafluorophosphate. *Green Chem.* **2003**, *5*, 361.
(31) Freire, M. G.; Neves, C. M. S. S.; Marrucho, I. M.; Coutinho, J. A. P.; Fernandes, A. M. Hydrolysis of Tetrafluoroborate and Hexafluorophosphate Counter Ions in Imidazolium-Based Ionic Liquids†. *J. Phys. Chem. A* **2010**, *114*, 3744−3749.
(32) Ferreyra, D. D.; Correa, N. M.; Silber, J. J.; Falcone, R. D. The Effect of Different Interfaces and Confinement on the Structure of the Ionic Liquid 1-Butyl-3-Methylimidazolium Bis-(Trifluoromethylsulfonyl)Imide Entrapped in Cationic and Anionic Reverse Micelles. *Phys. Chem. Chem. Phys.* **2012**, *14*, 3460.
(33) Zheng, Y.; Eli, W.; Li, G. FTIR Study of Tween80/1-Butyl-3-Methylimidazolium Hexafluorophosphate/Toluene Microemulsions. *Colloid Polym. Sci.* **2009**, *287*, 871−876.
(34) Rao, V. G.; Mandal, S.; Ghosh, S.; Banerjee, C.; Sarkar, N. Ionic Liquid-in-Oil Microemulsions Composed of Double Chain Surface Active Ionic Liquid as a Surfactant: Temperature Dependent Solvent and Rotational Relaxation Dynamics of Coumarin-153 in [Py]-[TF2N]/[C4mim][AOT]/Benzene Microemulsions. *J. Phys. Chem. B* **2012**, *116*, 8210−8221.
(35) Fletcher, K. A.; Pandey, S. Surfactant Aggregation within Room-Temperature Ionic Liquid 1-Ethyl-3-Methylimidazolium Bis-(Trifluoromethylsulfonyl)Imide. *Langmuir* **2004**, *20*, 33−36.
(36) Li, J.; Zhang, J.; Gao, H.; Han, B.; Gao, L. Nonaqueous Microemulsion-Containing Ionic Liquid [Bmim][PF6] as Polar Microenvironment. *Colloid Polym. Sci.* **2005**, *283*, 1371−1375.
(37) Rahman, A.; Rahman, M. M.; Mollah, M. Y. A.; Susan, M. A. B. H. Dynamic Percolation and Swollen Behavior of Nanodroplets in 1-Ethyl-3-Methylimidazolium Trifluoromethanesulfonate/Triton X-100/Cyclohexane Microemulsions. *J. Phys. Chem. B* **2016**, *120*, 6995−7002.
(38) Gayet, F.; El Kalamouni, C.; Lavedan, P.; Marty, J.-D.; Brûlet, A.; Lauth-de Viguerie, N. Ionic Liquid/Oil Microemulsions as Chemical Nanoreactors. *Langmuir* **2009**, *25*, 9741−9750.
(39) Pramanik, R.; Sarkar, S.; Ghatak, C.; Rao, V. G.; Sarkar, N. Ionic Liquid Containing Microemulsions: Probe by Conductance, Dynamic Light Scattering, Diffusion-Ordered Spectroscopy NMR Measurements, and Study of Solvent Relaxation Dynamics. *J. Phys. Chem. B* **2011**, *115*, 2322−2330.
(40) Pramanik, R.; Sarkar, S.; Ghatak, C.; Rao, V. G.; Setua, P.; Sarkar, N. Microemulsions with Surfactant TX100, Cyclohexane, and an Ionic Liquid Investigated by Conductance, DLS, FTIR Measurements, and Study of Solvent and Rotational Relaxation within This Microemulsion. *J. Phys. Chem. B* **2010**, *114*, 7579−7586.
(41) Kline, S. R. Reduction and Analysis of SANS and USANS Data Using IGOR Pro. *J. Appl. Crystallogr.* **2006**, *39*, 895−900.
(42) *Neutrons, X-rays, and Light: Scattering Methods Applied to Soft Condensed Matter*, 1st ed.; Lindner, P., Zemb, T., Eds.; North-Holland Delta Series; Elsevier: Amsterdam, Boston, 2002.
(43) Pedersen, J. S. Analysis of Small-Angle Scattering Data from Colloids and Polymer Solutions: Modeling and Least-Squares Fitting. *Adv. Colloid Interface Sci.* **1997**, *70*, 171−210.
(44) Guinier, A.; Fournet, G.; Walker, C. B. *Small Angle Scattering of X-rays*; J. Wiley & Sons: New York, 1955.
(45) Teubner, M.; Strey, R. Origin of the Scattering Peak in Microemulsions. *J. Chem. Phys.* **1987**, *87*, 3195−3200.
(46) Cheng, S.; Zhang, J.; Zhang, Z.; Han, B. Novel Microemulsions: Ionic Liquid-in-Ionic Liquid. *Chem. Commun.* **2007**, 2497.
(47) Eastoe, J.; Gold, S.; Rogers, S. E.; Paul, A.; Welton, T.; Heenan, R. K.; Grillo, I. Ionic Liquid-in-Oil Microemulsions. *J. Am. Chem. Soc.* **2005**, *127*, 7302−7303.
(48) Hyde, S.; Blum, Z.; Landh, T.; Lidin, S.; Ninham, B. W.; Andersson, S.; Larsson, K. *The Language of Shape: The Role of Curvature in Condensed Matter: Physics, Chemistry and Biology*; Elsevier, 1996.
(49) Rojas, O.; Tiersch, B.; Rabe, C.; Stehle, R.; Hoell, A.; Arlt, B.; Koetz, J. Nonaqueous Microemulsions Based on N,N′-Alkylimidazolium Alkylsulfate Ionic Liquids. *Langmuir* **2013**, *29*, 6833−6839.
(50) Berne, B. J.; Pecora, R. *Dynamic Light Scattering: With Applications to Chemistry, Biology, and Physics*, Dover ed.; Dover Publications: Mineola, NY, 2000.
(51) Koppel, D. E. Analysis of Macromolecular Polydispersity in Intensity Correlation Spectroscopy: The Method of Cumulants. *J. Chem. Phys.* **1972**, *57*, 4814−4820.
(52) Falcone, R. D.; Silber, J. J.; Correa, N. M. What Are the Factors That Control Non-Aqueous/AOT/n-Heptane Reverse Micelle Sizes? A Dynamic Light Scattering Study. *Phys. Chem. Chem. Phys.* **2009**, *11*, 11096.
(53) Rutkowski, C. A.; Williams, L. M.; Haines, T. H.; Cummins, H. Z. The Elasticity of Synthetic Phospholipid Vesicles Obtained by Photon Correlation Spectroscopy. *Biochemistry* **1991**, *30*, 5688−5696.
(54) Eyssautier, J.; Levitz, P.; Espinat, D.; Jestin, J.; Gummel, J.; Grillo, I.; Barré, L. Insight into Asphaltene Nanoaggregate Structure Inferred by Small Angle Neutron and X-Ray Scattering. *J. Phys. Chem. B* **2011**, *115*, 6827−6837.
(55) *Small Angle X-ray Scattering*; Glatter, O., Kratky, O., Eds.; Academic Press: London, New York, 1982.
(56) Wagner, J.; Härtl, W.; Hempelmann, R. Characterization of Monodisperse Colloidal Particles: Comparison between SAXS and DLS. *Langmuir* **2000**, *16*, 4080−4085.
(57) Leitão, H.; Telo da Gama, M. M.; Strey, R. Scaling of the Interfacial Tension of Microemulsions: A Landau Theory Approach. *J. Chem. Phys.* **1998**, *108*, 4189−4198.
(58) Schubert, K.-V.; Strey, R.; Kline, S. R.; Kaler, E. W. Small Angle Neutron Scattering near Lifshitz Lines: Transition from Weakly Structured Mixtures to Microemulsions. *J. Chem. Phys.* **1994**, *101*, 5343−5355.

DOI: 10.1021/acs.langmuir.8b02420
Langmuir 2018, 34, 12609−12618

(59) Koehler, R. D.; Schubert, K.-V.; Strey, R.; Kaler, E. W. The Lifshitz line in binary systems: Structures in water/C4E1 mixtures. *J. Chem. Phys.* **1994**, *101*, 10843−10849.
(60) Engelskirchen, S.; Elsner, N.; Sottmann, T.; Strey, R. Triacylglycerol microemulsions stabilized by alkyl ethoxylate surfactants-A basic study. *J. Colloid Interface Sci.* **2007**, *312*, 114−121.
(61) D'Arrigo, G.; Giordano, R.; Teixeira, J. Small-Angle Neutron Scattering Studies of Aqueous Solutions of Short-Chain Amphiphiles. *Eur. Phys. J. E: Soft Matter Biol. Phys.* **2003**, *10*, 135−142.
(62) Pal, A.; Esumi, K.; Pal, T. Preparation of Nanosized Gold Particles in a Biopolymer Using UV Photoactivation. *J. Colloid Interface Sci.* **2005**, *288*, 396−401.
(63) Murgia, S.; Palazzo, G.; Mamusa, M.; Lampis, S.; Monduzzi, M. Aerosol-OT in Water Forms Fully-Branched Cylindrical Direct Micelles in the Presence of the Ionic Liquid 1-Butyl-3-Methylimidazolium Bromide. *Phys. Chem. Chem. Phys.* **2011**, *13*, 9238.

DOI: 10.1021/acs.langmuir.8b02420
Langmuir 2018, 34, 12609−12618